# Optimum Design of Sensorless-Oriented IPMSM Considering Torque Characteristics

Min-Ro Park[1], Kyoung-Soo Cha[1], Jae-Woo Jung[2], and Myung-Seop Lim[1]

[1]Department of Automotive Engineering, Hanyang University, Seoul 04763, South Korea
[2]Division of Electric Powertrain, Hyundai Mobis Company Ltd., Yongin 16891, South Korea

**This article presents the design process of a sensorless-oriented interior permanent-magnet synchronous motor (IPMSM) with concentrated winding, based on spatial saliency for the traction motor in electric vehicles. The purpose of the design method is to ultimately achieve both stable rotor position detection and acceptable torque characteristics such as cogging torque and torque ripple. First, the relationship between the sensorless controllability and the electromagnetic parameters is derived through a mathematical method for a design considering sensorless drive of the motor. After describing the evaluating procedure of the sensorless controllability, the effects of the stator chamfer and notch are analyzed to figure out their effectiveness on the sensorless drive. Focusing on the analysis results of the geometric parameters, the improved model is designed through optimization, considering both sensorless controllability and torque characteristics. Response surface methodology (RSM) is used for optimization. Then, the machine characteristics including the sensorless controllability as the simulation results of the prototype and improved model are compared. It was found that the accuracy of the rotor position estimation and torque characteristics are improved simultaneously by means of the optimum design. Finally, the validity of the simulation results is verified by comparison with the test results of the prototype.**

*Index Terms*— **Cogging torque, high-frequency injection, saliency, sensorless control, torque ripple.**

## I. Introduction

THESE days, an interior permanent-magnet synchronous motor (IPMSM) is generally used for electric vehicle (EV) traction because of its high torque density. A position sensor is essential for vector control to achieve the maximum performance of the machine. However, this addition increases the system cost, volume, and complexity. In addition, using the position sensor could be a latent critical defect of an IPMSM, especially, for a traction application. To avoid this situation and to secure the fault safety, the design method of an IPMSM for sensorless drive is critical.

In an IPMSM, permanent magnets (PMs) have an effect on not only induced back EMF but also spatial saliency distribution. The non-uniformly positioned PM in the rotor causes a discrepancy between the $d$- and $q$-axis impedance. This is because the $d$-axis flux path is saturated easily by the magnetic flux and the high $d$-axis reluctance due to the low permeability of the PM. This result brings about the spatial saliency. Therefore, with a high-frequency signal injection method, the position of the rotor can be estimated based on the saliency [1]. As shown in Fig. 1, if the voltage injection angle is 0° when the voltage is injected on the $d$-axis, the $d$-axis self-inductance has a minimum value and the $d$- and $q$-axis mutual inductance must be zero because of the impedance. However, it is not easy to estimate the rotor position under load conditions, because the inductance is distorted by the input current or cross-coupling effect [2]–[6]. Thus, sensorless drive feasibility is predicted by analyzing the $d$- and $q$-axis inductances varied with a rotor position [4].

Manuscript received August 19, 2019; revised October 16, 2019; accepted October 21, 2019. Date of current version December 20, 2019. Corresponding author: M.-S. Lim (e-mail: myungseop@hanyang.ac.kr).

Color versions of one or more of the figures in this article are available online at http://ieeexplore.ieee.org.

Digital Object Identifier 10.1109/TMAG.2019.2949613

In this article, to evaluate the sensorless controllability, the relationship between the rotor position error and the electromagnetic parameters is mathematically derived. The rotor position error is estimated by the total harmonic distortion (THD) of the phase inductance and the waveforms of $d$- and $q$-axis self- and mutual inductances. In addition, based on electromagnetic computation, the optimum design for stable sensorless control and torque characteristic improvement is carried out. Some design factors, notch, chamfer, and pole angle are analyzed. Through the design optimization of the parameters, an improved model is proposed, fulfilling sensorless drivability and low cogging torque/torque ripple. Finally, the validity of the simulation results is verified by comparison with the experimental results of the prototype.

## II. Estimation Method of Sensorless Drive Feasibility

### A. Fixed Permeability Method

The fixed permeability method is used for calculating the inductances [7]. The first step is the finite-element analysis (FEA) including PMs. At this time, the nonlinear FEA has to be done, considering the saturation of the core. The next step is fixing the permeability of each element. After this, the linear FEA is conducted by eliminating the PM. At this point, by applying the one phase coil with the unit current, the self- and mutual inductance can be obtained. This process should be iterated by rotating the rotor, because the waveform of the $d$- and $q$-axis inductance is varied with the rotor position.

### B. Matrix Transformation of Inductance

With (1), a three-phase inductance matrix determined by the fixed permeability method can be transformed to $d$- and $q$-axis inductances depending on the voltage injection angle

$$L_{dq}^{r} = \frac{3}{2} T_{\theta_r} T_{dq} L_{abc} (T_{\theta_r} T_{dq})^{T} = \begin{bmatrix} L_d & L_{dq} \\ L_{qd} & L_q \end{bmatrix} \quad (1)$$

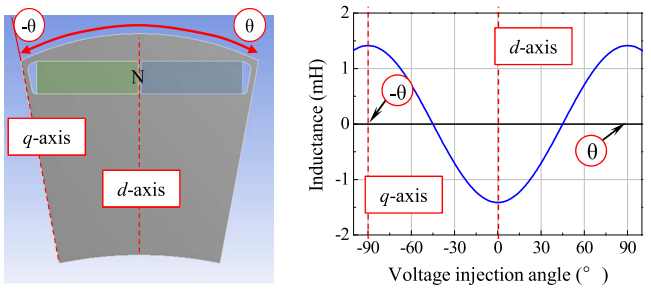


Fig. 1. $d$-axis inductance waveform under the no-load condition.

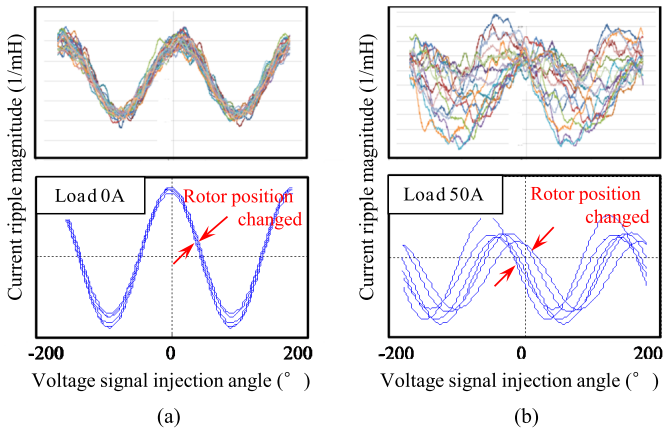


Fig. 2. Estimated current ripple (lower) and experimental result (upper). (a) No-load condition. (b) 50-A load condition.

where $L_{abc}$ is the three-phase inductances including spatial harmonics. $T_{dq}$ and $T_{\theta r}$ are the $d$- and $q$-axis transform and the rotational transform coefficient, respectively. $L_d$, $L_q$, $L_{dq}$, and $L_{qd}$ are the $d$- and $q$-axis self- and mutual inductances. Fig. 2 illustrates the variation in the $d$-axis current ripple (inversely proportional to $L_d$) with the rotor position under no-load and load conditions.

The harmonic term of the phase inductances, $L_{abch}$, is expressed mathematically as (2) to analytically determine the effect of the phase inductance harmonics on the $d$- and $q$-axis inductances. $n$ is the harmonic order of the phase inductances, and $L_h$ is an unknown value, as the magnitude of the harmonics. $L_{abch}$ can be transformed into $d$- and $q$-axis inductances

$$L_{abch} = L_h \begin{bmatrix} \cos 2\theta_r n & \cos 2n(\theta_r - \pi/3) & \cos 2n(\theta_r + \pi/3) \\ \cos 2n(\theta_r - \pi/3) & \cos 2n(\theta_r + \pi/3) & \cos 2\theta_r n \\ \cos 2n(\theta_r + \pi/3) & \cos 2\theta_r n & \cos 2n(\theta_r - \pi/3) \end{bmatrix}. \quad (2)$$

The $d$- and $q$-axis inductance harmonics caused by the phase inductance harmonics can be obtained using (1) and (2)

$$L^r_{dqh} = \frac{3}{2} L_h \begin{bmatrix} +\cos 6\theta_r m & -\sin 6\theta_r m \\ -\sin 6\theta_r m & -\cos 6\theta_r m \end{bmatrix} \quad @n = 3m - 1$$
$$L^r_{dqh} = \frac{3}{2} L_h \begin{bmatrix} +\cos 6\theta_r m & +\sin 6\theta_r m \\ +\sin 6\theta_r m & -\cos 6\theta_r m \end{bmatrix} \quad @n = 3m + 1$$
$$L^r_{dqh} = 0 \quad @n = 3m \quad (3)$$

where $m$ is a natural number. As described in (3), the harmonics of the phase inductances, except the $3k$th harmonic terms, cause the $6k$th periodic ripple of the $d$- and $q$-axis inductances varied with the rotor position during one period in electrical angle ($k = 1, 2, 3, \ldots$). The relationship between the harmonics of the phase inductances and the $d$- and $q$-axis inductances can be organized simply as Table I [8]. In addition, to verify the mathematical process, the variations in the inductance waveforms are illustrated in the simulation results as shown in Fig. 3. When the fourth harmonics exist in the phase inductance, the $d$- and $q$-axis mutual inductance has six-periodic ripple during one period in electrical angle according to the rotor position. On the other hand, when the fifth harmonics exist in the phase inductance, the mutual inductance has 12-periodic ripple. It shows that the relationship between the phase inductance harmonics and the variations in the $d$- and $q$-axis mutual inductance waveforms is conformed to Table I. Therefore, the magnitude of the estimation error is represented as well by examining the phase inductance THD, except the $3k$th harmonic terms.

TABLE I
RELATION BETWEEN THE HARMONIC ORDERS OF THE PHASE INDUCTANCES AND THE $d$- AND $q$-AXIS MUTUAL INDUCTANCES

| $n$ | 2 | 4 | 5 | 7 | 8 | 10 | 11 | 13 | … |
|---|---|---|---|---|---|---|---|---|---|
| $m$ | 1 | 1 | 2 | 2 | 3 | 3 | 4 | 4 | … |
| $L_{dqh}$ | 6 | 6 | 12 | 12 | 18 | 18 | 24 | 24 | $6k$-th |

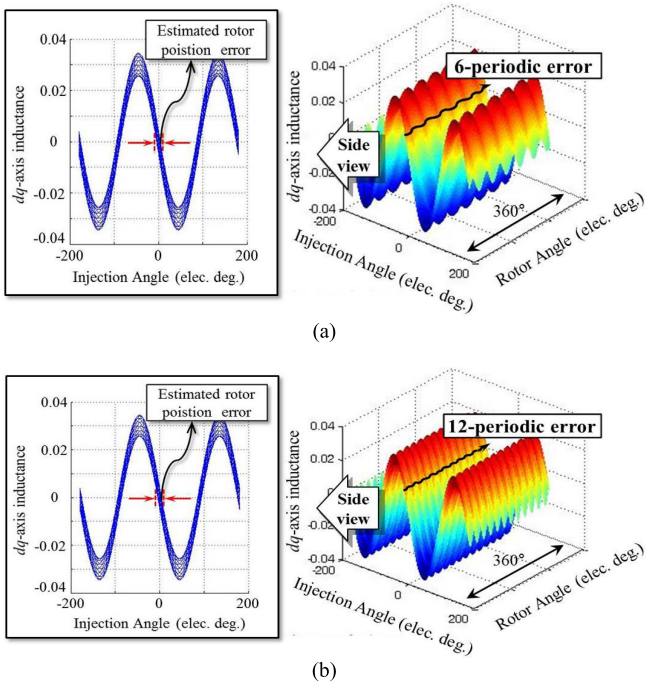


Fig. 3. $6k$th-order harmonics of the $d$- and $q$-axis inductances caused by the phase inductance harmonics. (a) Fourth harmonics (15%) of phase inductance injected, $n = 4$. (b) Fifth harmonics (15%) of phase inductance injected, $n = 5$.

## III. ANALYSIS OF THE DESIGN PARAMETERS AND PROTOTYPE

### A. Analysis of Design Parameters for Sensorless Drive

In this article, the chamfer and notch in the stator tooth-tip are analyzed to find out their effects on a sensorless controllability of IPMSM. For quantification of sensorless

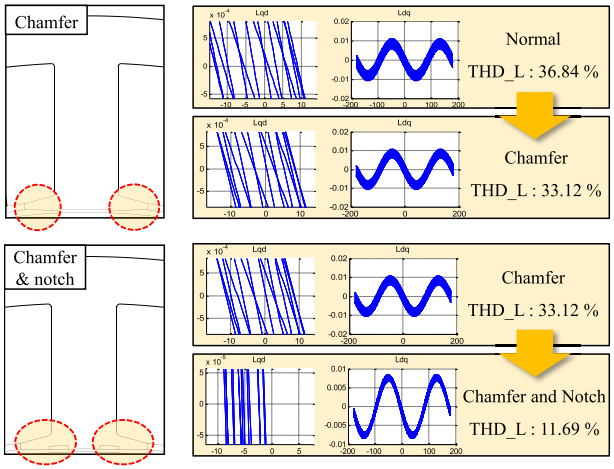


Fig. 4. Design factors and the $dq$-axis inductances (THD_L: phase inductance THD).

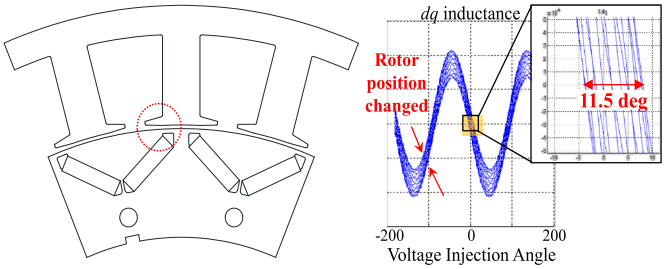


Fig. 5. Sensorless-oriented prototype (left) and the variation $L_{dq}$ waveforms with the rotor position (electrical angle: 0°–180°) (right).

control feasibility, the phase inductance THD, except the $3k$th harmonic terms, is used. This is because the phase inductance spatial harmonics cause variation in $L_d$, $L_q$, $L_{dq}$, and $L_{qd}$ waveforms with the rotor position. The results of FEA under the load conditions are described in Fig. 4. The point is that the chamfer and notch have a positive effect on the sensorless control. Given this analysis, it is inferred that the shape of the tooth-tip in the stator is closely related to the performance of the saliency-based sensorless drive. Therefore, it shows that the shape and saturation of the stator tooth-tip is one of the key factors for concentrated winding sensorless drive machine.

### *B. Analysis of a Prototype*

A prototype, conventional traction motor with chamfer only is shown in Fig. 5. Fig. 5 also illustrates the variation in $L_{dq}$ waveform with the rotor position under the maximum load conditions. It is expected that the sensorless control for the prototype is viable because the variation level of $L_{dq}$ is not high. However, the shape and saturation of the tooth-tip as well as the combination of the slot open and pole angle cause its high cogging torque and torque ripple (cogging torque; peak to peak: 14.96 Nm, torque ripple: 12.92%). For optimizing the machine, the design parameters affecting not only the sensorless controllability but also the cogging torque and torque ripple are analyzed.

## IV. Improved Design

### *A. Optimization*

In this study, through the FEA-based electromagnetic computation, the optimal design for the stable sensorless control and improved torque characteristics is carried out. The statistical experimental methods such as design of experiment (DOE)

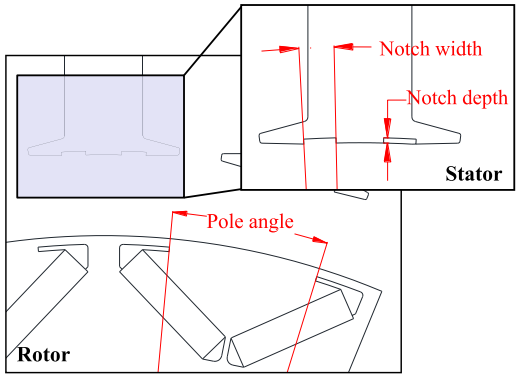


Fig. 6. Design parameters for DOE.

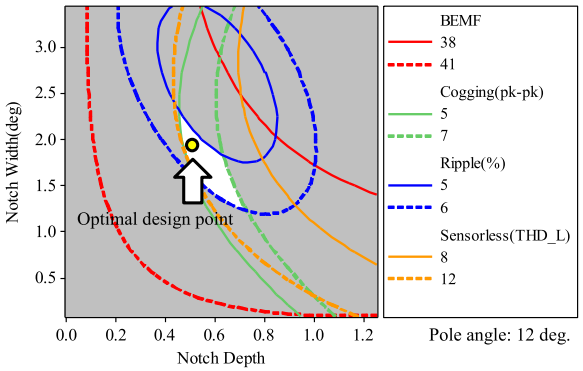


Fig. 7. Result of the RSM and the target region of the design parameters.

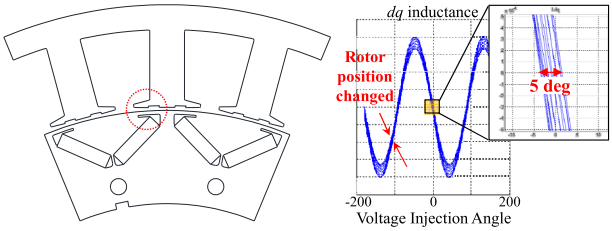


Fig. 8. Improved model (left) and the variation $L_{dq}$ waveforms with the rotor position (electrical angle: 0°–180° degree) (right).

and response surface methodology (RSM) are applied for the optimization. The RSM is a statistical method to solve the electromagnetic problem of multivariate using the reasonable DOE. This methodology evaluates the effects of various parameters and searches for optimal conditions [9], [10]. The notch width and depth, and pole angle were selected as the optimal design parameters for the RSM as shown in Fig. 6. In addition, the objective functions are back electromotive force (BEMF), phase inductance THD, cogging torque, and torque ripple. To find the optimal design point, the surrogate model was built by fitting the function considering the relationship between the design parameters and objective functions. Fig. 7 describes the results of RSM. The white area in the figure is the optimal design region. The values of the parameters meet the requirements (optimal design point) that should be decided in that area.

### *B. Improved Design Result*

The improved model as the results of the optimization and the $d$- and $q$-axis inductances under the maximum load conditions is shown in Fig. 8. The values of the optimal parameters are as follows: pole angle: 12°, notch width: 1.90°, and

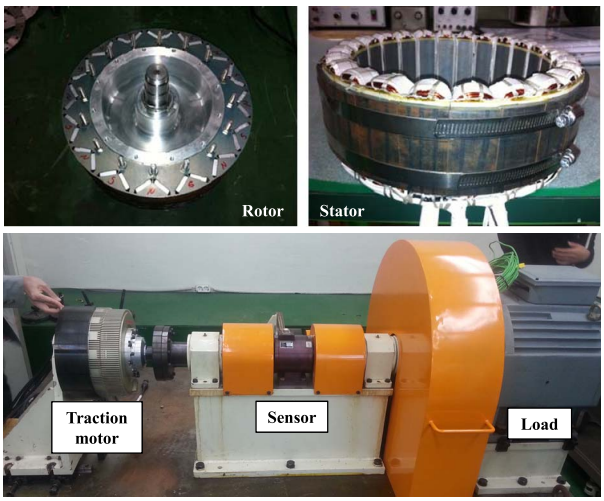


Fig. 9. Photograph of the prototype and test set.

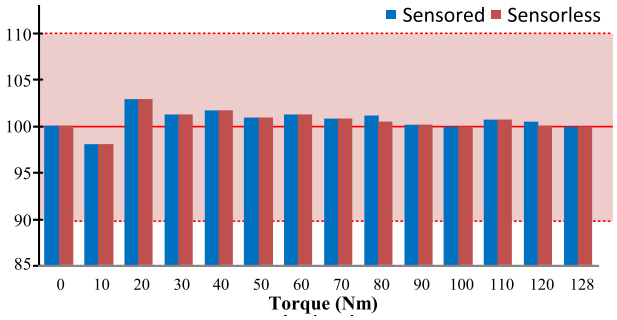


Fig. 10. Torque accuracy test at 200 rpm of the prototype [$y$-axis: torque accuracy (%)].

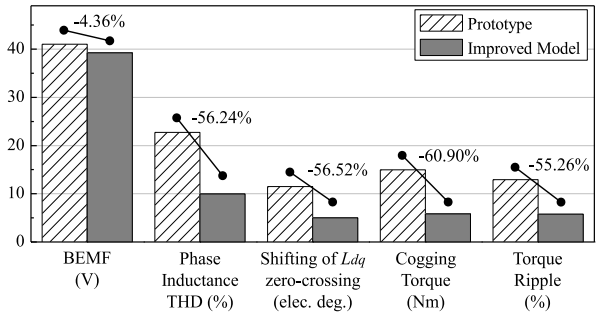


Fig. 11. Comparison between the prototype and improved model.

TABLE II
FEA AND EXPERIMENTAL RESULTS OF THE PROTOTYPE (25 C)

| | BEMF [V] | Cogging torque [Nm] |
|---|---|---|
| FEA | 44.60 | 21.38 |
| Experiment | 45.33 | 20~22 |

notch depth: 0.56 mm. The rotor position could be estimated more precisely than the prototype, thanks to hardly shifting zero-crossing points of $L_{dq}$. Furthermore, the improved model has much lower cogging torque and torque ripple (cogging torque; peak to peak: 5.85 Nm, torque ripple: 5.78%).

## V. VERIFICATIONS

The prototype is fabricated as shown in Fig. 9. It was tested to verify the validity of the simulation results. The no-load test results are shown in Table II. Given the torque test results in Fig. 10, the output torques are slightly different when the machine is operated by sensored and sensorless drive. Finally, the characteristics of the improved model and the prototype are compared in Fig. 11.

## VI. CONCLUSION

In this article, the design method of saliency-based sensorless-controlled IPMSM with concentrated winding is suggested. First, the electromagnetic parameters for evaluating the sensorless controllability are obtained from the mathematical methods. These parameters are the THD of the phase inductance and the waveforms of $d$- and $q$-axis self- and mutual inductance. In addition, the design parameters are examined to clarify the design method of sensorless controlled IPMSM with concentrated winding. As a result, the shape and saturation of the tooth-tip is one of the key factors for designing a sensorless-oriented motor. However, the saturation of the tooth-tip gives rise to high cogging torque and torque ripple. Hence, to improve the sensorless controllability and torque characteristics, the RSM is conducted using the FEA-based electromagnetic computation with the design parameters such as notch size and pole angle. Consequently, not only the cogging torque and torque ripple decreased by about 61% and 55% but also the shifting of the $d$- and $q$-axis inductances' zero-crossing or phase inductance THD, representing sensorless drive feasibility, is reduced by 56%.

## ACKNOWLEDGMENT

Thi work was supported by the National Research Foundation of Korea (NRF) grant funded by the Korean Government (MSIP; Ministry of Science, ICT & Future Planning) under Grant 2018R1C1B5085447.

## REFERENCES

[1] S. Kim, J.-I. Ha, and S.-K. Sul, "PWM switching frequency signal injection sensorless method in IPMSM," *IEEE Trans. Ind. Appl.*, vol. 48, no. 5, pp. 1576–1587, Sep./Oct. 2012.

[2] Y. Kano, T. Kosaka, N. Matsui, and M. Fujitsuna, "Sensorless-oriented design of concentrated-winding IPM motors for HEV drive application," in *Proc. ICEM*, Sep. 2012, pp. 2709–2715.

[3] Y. Li, Z. Q. Zhu, D. Howe, and C. M. Bingham, "Modeling of cross-coupling magnetic saturation in signal-injection-based sensorless control of permanent-magnet brushless AC motors," *IEEE Trans. Magn.*, vol. 43, no. 6, pp. 2552–2554, Jun. 2007.

[4] Z. Q. Zhu, Y. Li, D. Howe, and C. M. Bingham, "Compensation for rotor position estimation error due to cross-coupling magnetic saturation in signal injection based sensorless control of PM brushless AC motor," in *Proc. IEMDC*, May 2007, pp. 208–213.

[5] N. Bianchi and S. Bolognani, "Influence of rotor geometry of an IPM motor on sensorless control feasibility," *IEEE Trans. Ind. Appl.*, vol. 43, no. 1, pp. 87–96, Jan./Feb. 2007.

[6] R. Wrobel *et al.*, "Rotor design for sensorless position estimation in permanent-magnet machines," *IEEE Trans Ind. Electron.*, vol. 58, no. 9, pp. 3815–3824, Sep. 2011.

[7] M.-S. Lim, S.-H. Chai, and J.-P. Hong, "Design of saliency-based sensorless-controlled IPMSM with concentrated winding for EV traction," *IEEE Trans. Magn.*, vol. 52, no. 3, Mar. 2016, Art. no. 8200504.

[8] M.-S. Lim, S.-H. Chai, and J.-P. Hong, "Design and iron loss analysis of sensorless-controlled interior permanent magnet synchronous motors with concentrated winding," *IET Electr. Power Appl.*, vol. 8, no. 9, pp. 349–356, Nov. 2014.

[9] B.-H. Lee, J.-P. Hong, and J.-H. Lee, "Optimum design criteria for maximum torque and efficiency of a line-start permanent-magnet motor using response surface methodology and finite element method," *IEEE Trans. Magn.*, vol. 48, no. 2, pp. 863–866, Feb. 2012.

[10] J. T. Li, Z. J. Liu, M. A. Jabbar, and X. K. Gao, "Design optimization for cogging torque minimization using response surface methodology," *IEEE Trans. Magn.*, vol. 40, no. 2, pp. 1176–1179, Mar. 2004.